ADVANCED MATERIALS
www.advmat.de

On-Chip Active Non-Reciprocal Topological Photonics

*Ridong Jia, Thomas Caiwei Tan, Sobhan Subhra Mishra, Wenhao Wang, Yi Ji Tan, and Ranjan Singh**

Chip-scale non-reciprocity is essential for advancing integrated photonics, particularly in realizing photonic circulators and isolators for data communication, signal modulation, and quantum computing. However, achieving a non-reciprocal silicon chip with a small footprint, high isolation ratio, low loss, and active control remains a challenge. Here, a non-reciprocal topological silicon chip based on magneto-optical Indium Antimonide (InSb) integrated valley Hall system is reported. The valley-conserved non-reciprocal modes, realized by breaking both time-reversal and spatial-inversion symmetries, enable ultra-compact and efficient non-reciprocal photonic devices that outperform conventional chips. A maximum isolation ratio of 64.3 dB and a low chip loss of 2.6 dB is experimentally achieved by fine-tuning the non-reciprocal critical coupling points of a topological cavity with a small footprint of $6.4 \times 2.5\lambda^2$. An all-optical method is also applied to actively modulate the isolation ratio from 0 to 48 dB. The development of a non-reciprocal topological silicon chip marks a pivotal advancement in communication systems, LiDAR, terahertz technologies, quantum computing, and cryptography.

1. Introduction

Photonic non-reciprocity refers to the asymmetric propagation of electromagnetic waves in opposite directions, a phenomenon first observed through the Faraday effect in 1845. Over the past century, non-reciprocal devices such as wave circulators and isolators have become essential in modern electromagnetics. Achieving photonic non-reciprocity typically involves breaking time-reversal symmetry via magneto-optical (MO) effects,[1–8] acousto-optical (AO) effects,[9–13] optomechanical effects,[14,15] or time-reversal-symmetry conserved approaches[16] including dynamic electrical modulation[17] and optical nonlinearity.[18–20] Integrating non-reciprocity into a photonic integrated circuit (PIC)[21] chip holds significant potential for advancements in quantum computing, telecommunication, and signal modulation. However, achieving a high isolation ratio in a miniaturized footprint with minimal non-reciprocal loss remains a challenge. Large chip space and long waveguides are often necessary to integrate bulky non-reciprocal elements to enhance weak non-reciprocal effects such as in AO isolators.[12,13] Moreover, considerable material losses from the non-reciprocal elements, like yttrium iron garnet,[2] can substantially reduce chip efficiency, especially in extended interaction areas. Additionally, the intrinsic bending limitations of conventional PIC waveguides require an increased chip footprint to avoid propagating losses at bending corners. Therefore, developing a compact, low-loss PIC platform with effectively integrated non-reciprocal elements is crucial for advancing non-reciprocal chip technology.

The emergence of topological photonic integrated circuits in telecom[22] and terahertz[23] bands (T^2PICs) provides a robust and compact platform that enables efficient waveguide bending and chip miniaturization. Achieving non-reciprocity on these topological chips promises to enhance both compactness and efficiency. While one-way propagation has been observed in quantum Hall photonic crystals,[1,24,25] translating this type of non-reciprocity into a compact, efficient, and low-cost chip remains challenging. This difficulty arises from the fabrication complexities in scaling MO structures to the micrometer and nanometer levels, as well as the need to mitigate significant losses from scattering and material absorption.[26] Valley photonic crystal (VPC) chips,[27–36] which break spatial-inversion symmetry through manipulating the geometric holes or pillars on a 2D isotropic slab, eliminate the difficulty in realizing low-loss MO structures and provide immunity to losses from waveguide bending and defect scattering. VPC waveguide modes also

R. Jia, T. C. Tan, S. S. Mishra, W. Wang, Y. J. Tan
Division of Physics and Applied Physics
School of Physical and Mathematical Sciences
Nanyang Technological University
Singapore 637371, Singapore
R. Jia, T. C. Tan, S. S. Mishra, W. Wang, Y. J. Tan
Centre for Disruptive Photonic Technologies
Nanyang Technological University
Singapore 639798, Singapore
R. Singh
Department of Electrical Engineering
University of Notre Dame
Notre Dame, IN 46556, USA
E-mail: rsingh3@nd.edu

The ORCID identification number(s) for the author(s) of this article can be found under https://doi.org/10.1002/adma.202501711

DOI: 10.1002/adma.202501711

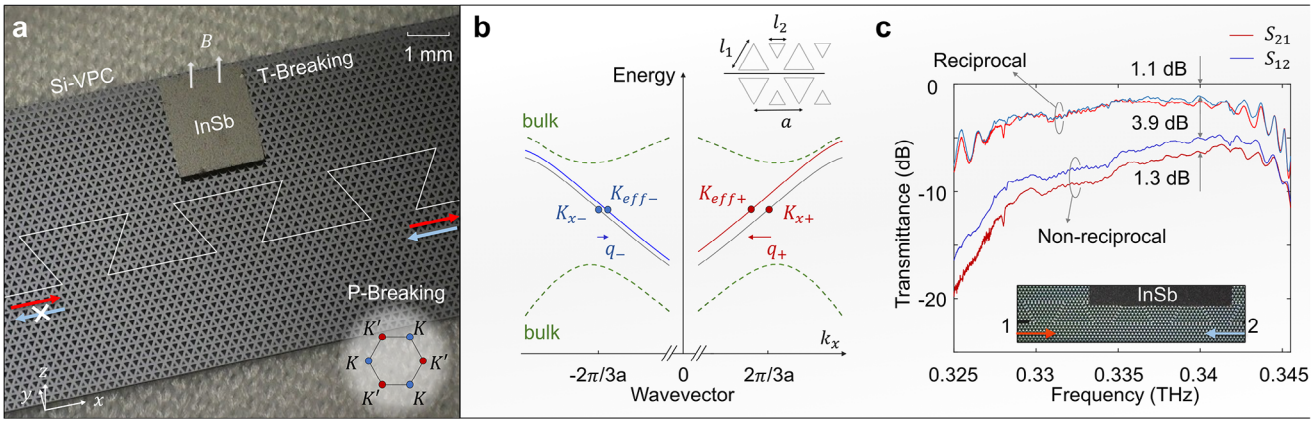

Figure 1. Valley-conserved non-reciprocal topological silicon chip. a) Image of the non-reciprocal silicon topological chip integrated with InSb. Forward (red) and backward (blue) propagations are non-reciprocal and topology-protected, achieved by breaking the spatial and temporal reversal symmetries (P- and T-breaking). The bottom right inset shows the first Brillouin zone of the VPC, with differentiated *K* and *K'* valleys. b) Band diagrams of the reciprocal (gray band) and non-reciprocal (red and blue bands) topological edge states for the silicon VPCs with or without InSb under a magnetic field, respectively. $K_{x\pm}$ indicate the reciprocal momenta and $K_{eff\pm}$ are the effective non-reciprocal momenta, with momentum deviations of $q_\pm$. The zigzag interface is shown in the top right inset. c) Image and experimental transmittance spectra for the non-reciprocal 16-bend topological waveguide. S_{21} (red) and S_{12} (blue) are reciprocal for pure Si-VPC while exhibiting a 1.3 dB difference (0.34 THz) for the non-reciprocal chip.

allow flexible on-chip integration by offering tunable waveguide crosstalk from sub-λ to multi-λ (λ indicates wavelength in free space) coupling distances.[37] Incorporating broken time-reversal symmetry into these VPC chips would achieve topology-protected non-reciprocity in the valley Hall system. The resulting valley-conserved non-reciprocal modes can introduce the numerous advantages of VPC into non-reciprocal devices. Ultra-compact non-reciprocal chips become achievable due to the nearly arbitrary waveguide routing and the tunability of waveguide coupling. The efficiency of these non-reciprocal chips is significantly enhanced by minimized chip loss, potentially surpassing conventional systems lacking topological robustness.[5,6,15] Furthermore, such non-reciprocal T^{2}PIC devices are built on complementary metal-oxide-semiconductor (CMOS)-compatible substrates such as silicon and its compounds, expanding their application potential.

Here, we demonstrate on-chip topological non-reciprocity by aligning the MO crystal InSb onto a terahertz VPC silicon chip. A valley-conserved non-reciprocal mode is thus achieved by breaking both the temporal and spatial reversal symmetries, enabling record chip compactness and efficiency. We demonstrate an on-chip topological isolator using a compact topological cavity measuring $6.4 \times 2.5\lambda^2$, achieving a maximum isolation ratio of 64.3 dB and a low chip loss of 2.6 dB. Adjusting the interaction volume between InSb and the cavity mode to manipulate the non-reciprocal critical coupling conditions allows for a tunable isolation ratio ranging from 0 to 64.3 dB. Moreover, the isolation ratio is controllable via an active optical pump, enabling modulation depths from 0 to 48 dB. Our topological non-reciprocal chip and its active control represent a significant advancement in non-reciprocal devices, promising applications in 6G to future XG terahertz wireless communication systems, LiDAR (light detection and ranging), quantum computer hardware architectures, and cryptography.

2. Results and Discussion

2.1. Valley-Conserved Non-Reciprocal Mode

Non-reciprocity in the VPC waveguide is achieved by breaking both the spatial-inversion and time-reversal symmetries (referred to as P-breaking and T-breaking). **Figure 1a** illustrates the sample image where InSb is integrated on top of the silicon VPC chip. The topological valley edge state in the silicon slab emerges at the interface of VPCs with opposite valley Chern numbers, achieved through breaking the C_6 spatial symmetry of the honeycomb lattice to C_3 symmetry[28,36] (P-breaking). This is achieved by altering the size of the on-site triangular air holes, distinguishing the *K* and *K'* valleys akin to valleytronics in 2D materials,[38] as shown by the first Brillouin zone in the bottom right inset of Figure 1a. At the zigzag interface of two mirrored VPC bulks, the topological edge state enables efficient routing over the sharp corners and defects due to the valley momentum conservation. On the other hand, T-breaking is achieved by the gyrotropic nature of InSb under an external magnetic bias *B* along *z*-direction. The MO effect introduces different effective permittivities of InSb along the $\pm x$ directions, expressed as $\epsilon_\pm = \epsilon_\pm' - i\epsilon_\pm''$, where $\epsilon_\pm'$ and $\epsilon_\pm''$ denote the real and imaginary permittivities related to the phase and loss of the propagating wave, respectively. The coupling between topological edge state and InSb gives rise to both P- and T-breaking, enabling valley-conserved non-reciprocal mode for topology-protected and non-reciprocal waveguiding.

The band diagram of the valley-conserved non-reciprocal mode is schemed in Figure 1b for the transverse-electric (TE) mode at the zigzag interface, where l_1 and l_2 indicate the side lengths of the equilateral triangles as $l_1 \neq l_2$ (top right inset). The time-reversal-invariant silicon structure leads to reciprocal $\pm x$-directional valley momenta as $|K_{x+}| = |K_{x-}|$ (gray band), while the coupling with InSb gives rise to the non-reciprocal effective

valley momenta $|K_{eff+}| \neq |K_{eff-}|$ (red and blue bands). The non-reciprocal momentum deviations are defined as $q_{\pm} = Re[K_{eff\pm} - K_{x\pm}]$ (Figure 1b) and the non-reciprocal attenuation coefficients are given by $\alpha_{\pm} = Im[K_{eff\pm} - K_{x\pm}]$, related to $\epsilon_{\pm}'$ and $\epsilon_{\pm}''$, respectively. The values of $q_{\pm}$ and $\alpha_{\pm}$ are determined by the coupling volume V_{InSb} between the edge state and InSb (see Section S1, Supporting Information) as well as the value of the magnetic bias B. We express $\alpha_{\pm}$ using non-reciprocal loss rates as $\gamma_{\pm}(\alpha_{\pm}) = \gamma_0 + \gamma_{MO\pm}(B)$, where γ_0 indicates the intrinsic reciprocal loss rate due to the free carriers in InSb, and $\gamma_{MO\pm}(B)$ are the non-reciprocal loss rates from the MO effect. It is noteworthy that $q_{\pm}$ and $\alpha_{\pm}$ are not linearly related, with the relationship dependent on V_{InSb} and the orientation of the waveguide.

The experimental transmittances of the non-reciprocal topological waveguides are shown in Figure 1c, indicated by power S-parameters S_{21} (from port 1 to port 2) and S_{12} (from port 2 to port 1). The sample image is displayed in the inset, where the air hole sizes are $l_1 = 0.65a = 157.6$ µm and $l_2 = 0.35a = 84.9$ µm with the lattice period $a = 242.5$ µm. Robust reciprocal waveguiding through sixteen 60° sharp corners is illustrated with the experimental transmittances reaching up to −1.1 dB. The out-of-plane magnetic field of $B = 0.632$ T gives rise to an experimental isolation ratio of $|S_{21} - S_{12}| = 1.3$ dB at 0.34 THz due to the non-reciprocal loss $\gamma_{\pm}$. An additional 3.9 dB chip loss is observed, which is mainly attributed to the reciprocal loss γ_0. Importantly, this non-reciprocity is observed across the entire topological band from 0.325 to 0.345 THz. Additional results of non-reciprocal waveguiding in various configurations are discussed in Section S2 (Supporting Information).

2.2. Non-Reciprocal Critical Coupling of Topological Isolator

Combining non-reciprocity with a topological cavity[39] enables an efficient on-chip topological isolator, significantly improving the isolation ratio, particularly at critical coupling conditions. This critical point signifies the complete energy transfer from the topological bus waveguide to the topological cavity, occurring when the intrinsic cavity loss rate γ_i (material absorption, in-plane scattering, and out-of-plane leakage) equals the cavity-waveguide coupling induced loss rate γ_c. In a reciprocal system, the clockwise (CW) and counterclockwise (CCW) cavity resonant modes are symmetric, reaching critical points at identical resonant frequencies f_{21} (CW) and f_{12} (CCW). Both the S_{21} (CW) and S_{12} (CCW) of the bus waveguide reach zero at this point, and their phase spectra $\angle S_{21}$ and $\angle S_{12}$ undergo a discontinuous 2π phase change with undefined gradients (detailed in Section S3, Supporting Information). In contrast, the CW and CCW modes of a topological isolator present detuned resonant frequencies $\Delta f = f_{21} - f_{12}$, due to the phase difference resulting from momentum deviations $q_{\pm}$. The non-reciprocal losses $\gamma_{\pm}$ lead to different coupling conditions for the CW and CCW modes, with the critical point of each maximizing the isolation ratios.

Figure 2a illustrates the simulated field profile $|\psi|^2$ (ψ indicates H_z for TE mode) of the on-chip topological cavity without InSb. The robust topological waveguides allow for a compact parallelogram resonator measuring $6.4 \times 2.5\lambda^2$. The length of the topological waveguide mode extent is 0.9λ (when $|\psi|^2$ is $1/e$ of its maximum at the interface), and the excitation distance between the waveguide and the cavity is 1.9λ. This 1.9λ distance ensures an over-coupling condition where $\gamma_i < \gamma_c$, such that the $\gamma_{+(-)}$ induces the non-reciprocal critical condition where $\gamma_i + \gamma_{+(-)} = \gamma_c$ by evanescently integrating InSb near the upper arm of the cavity (inset image). We showcase the experimental results of two different topological isolator configurations in Figure 2b. The isolation ratio in the left panel is 64.3 dB for an optimized V_{InSb} with Δf near to 0. The isolation background is −14.4 dB, also referred to as isolator insertion loss,[2] which can be optimized through detuning f_{21} and f_{12}. The right panel of Figure 2b illustrates the results with Δf of 120 MHz through adjusting V_{InSb}. The isolation ratio is 31.4 dB, and the isolation background is optimized to −10.3 dB which shows promise for further improvement such as improving V_{InSb} or B. Notably, the overall intrinsic losses of our non-reciprocal chips are 3.4 dB (left) and 2.6 dB (right), encompassing materials loss, waveguide propagating loss, bending loss, and terahertz input and output coupling losses. To the best of our knowledge, this 2.6 dB enabled by the topological silicon VPC platform is the lowest chip loss among the state-of-the-art isolators, as shown in **Table 1**, which also highlights our highest isolation ratio and smallest cavity size.

We showcase the formation of topological non-reciprocal critical points in Figure 2c, using experimental transmittance (S_{21} and S_{12}) and phase spectra ($\angle S_{21}$ and $\angle S_{12}$) for topological cavity without InSb for control (left), a topological isolator (with InSb) with B values of 0 T (mid-left), 0.632 T (mid-right), and −0.632 T (right). The over-coupling condition of the pure topological cavity (Figure 2a) is indicated by the negative gradients of $\angle S_{21}$ and $\angle S_{12}$. This over-coupling condition enables that the integration of InSb drives the reciprocal resonant mode to critical points where $\gamma_i + \gamma_0 = \gamma_c$. When $B = 0$ T, the transmittance depths of S_{21} and S_{12} become lower and $\angle S_{21}$ and $\angle S_{12}$ show faster phase transitions, indicating that both the CW and CCW modes are near to the critical points where $\gamma_i + \gamma_0 \approx \gamma_c$. When a 0.632 T bias is applied, the CCW mode (blue) reaches its critical point as $\gamma_i + \gamma_0 + \gamma_{MO-} = \gamma_c$, exhibiting an undefined gradient of $\angle S_{12}$ with a 2π phase shift. In contrast, CW mode (red) operates in the under-coupling regime as $\gamma_i + \gamma_0 + \gamma_{MO+} > \gamma_c$ with a positive phase gradient and a phase shift smaller than π. These coupling conditions are reversed when the magnetic bias is switched to the -z-direction at −0.632 T, where only the CW mode is critically coupled as shown in the right panel of Figure 2c.

Figure 2d illustrates the experimental evolution of the non-reciprocal spectra of S_{21} (red) and S_{12} (blue) with increasing B indicated by deepening colormaps. We tune V_{InSb} by aligning InSb and the topological chip properly to ensure a critical point for S_{21} at $B = 0.607$ T. The resonance frequencies detune from the reciprocal initial state (black) to the deep red and blue spectra with increasing Δf. CW mode (red) reaches its critical point when B rises to 0.607 T while the CCW mode (blue) remains over-coupled. Figure 2e,f highlights the evolution of the isolation ratio and Δf, respectively. Both the CW (red circle) and CCW (blue circle) isolation ratios increase with B, reaching the maxima of 37 and 14 dB (Figure 2e) at respective resonance frequencies f_{21} and f_{12}. Δf (green diamond) increases from 0 to 61 MHz (Figure 2f). In contrast, these values remain near to zero for the silicon VPC without InSb (orange square), indicating reciprocal features. Notably, the terahertz non-reciprocal waveguide and cavity modes remain predominantly confined within the silicon slab,[6]

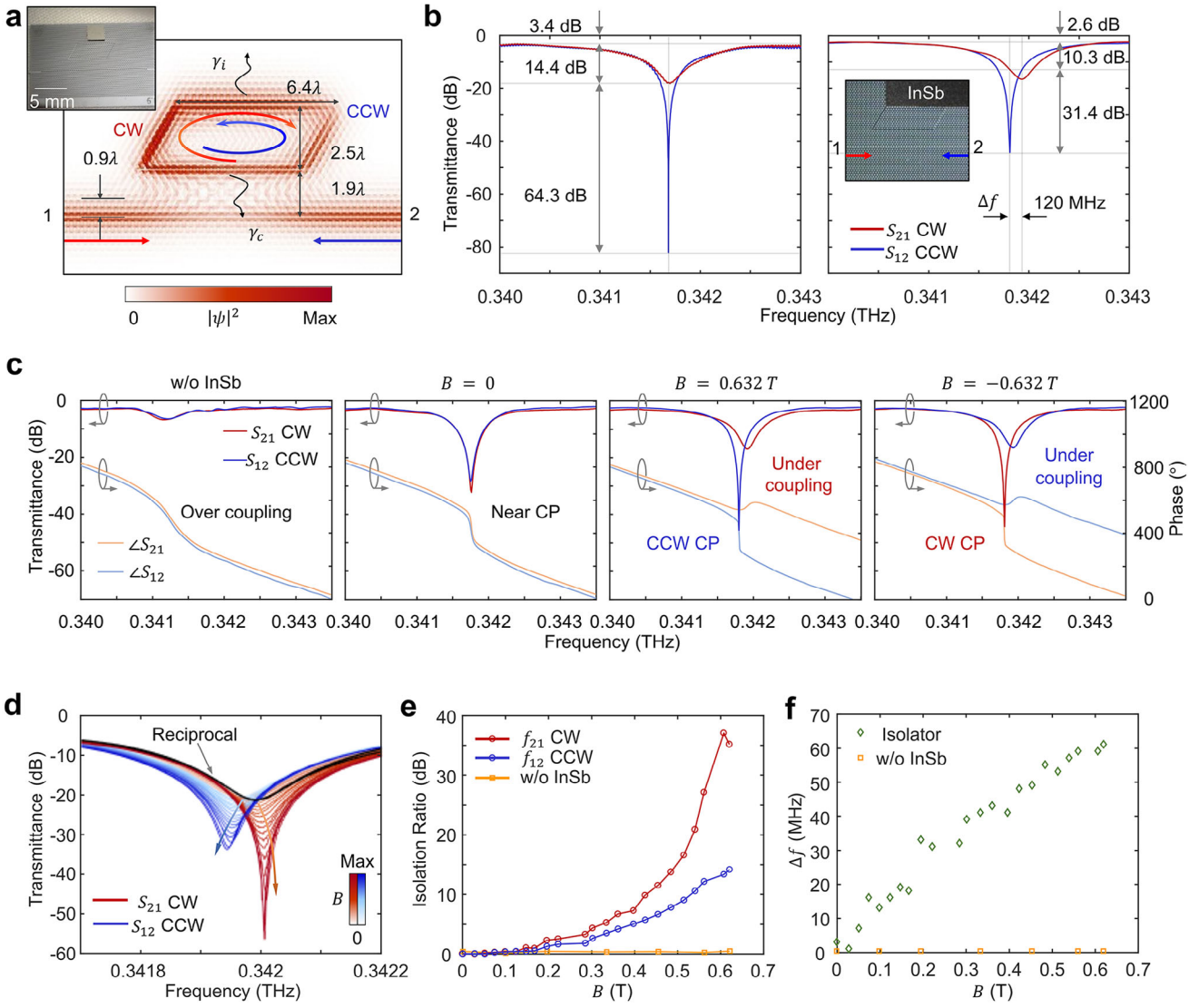

Figure 2. Performance of on-chip topological isolator. a) Sample image and simulated field profile $|\psi|^2$ of a silicon topological cavity. Waveguide mode tail is 0.9λ and cavity excitation distance is 1.9λ. γ_i and γ_c indicate intrinsic and coupling loss rates of the cavity. CW and CCW modes are indicated by S_{21} (red) and S_{12} (blue), respectively. b) Image and experimental results for topological isolators. CW and CCW modes are indicated by S_{21} (red) and S_{12} (blue), respectively. 64.3 dB isolation ratio (left) and 2.6 dB chip loss (right) are achieved, with frequency detuning Δf of 0 and 120 MHz, respectively. c) Experimental transmittance and phase spectra for topological cavity without InSb (left), and topological isolator at $B = 0$ T (mid-left), 0.632 T (mid-right), and −0.632 T (right), respectively. CP: critical point. d) Evolution of S_{21} (red) and S_{12} (blue) versus increasing value of B. The reciprocal reference is shown in black. e,f) Isolation ratios for CW (red circle) and CCW (blue circle) modes at respective resonance frequencies f_{12} and f_{21}, and frequency detuning Δf (green diamond) versus B. Reference results are indicated by orange squares for topological cavity without InSb.

resulting from the out-of-plane evanescent coupling with InSb. The non-reciprocal critical coupling conditions and isolation ratios are frequency-dependent, as γ_c exhibits dispersion due to the waveguide supercoupling mechanism[37] and γ_i is influenced by the intrinsic material dispersion of InSb.

Precise control of the coupling volume V_{InSb} allows for variable isolation ratios through different combinations of $q_{\pm}$ and $\gamma_{\pm}$, providing additional degrees of freedom in tuning non-reciprocity. For instance, both CW and CCW critical points can be observed at arbitrary B through optimizing V_{InSb}. **Figure 3a** illustrates the experimental results of $S_{12} - S_{21}$ for CW (red) and CCW (blue) modes, respectively, versus B from 0 to 0.62 T. The CW and CCW critical points are achieved at $B = 0.072$ T and 0.550 T, respectively, in contrast to the constant zero value for the reference cavity without InSb (gray). Figure 3b,c highlights the transmittance and phase spectra, respectively, when B equals 0.026, 0.072, 0.218, and 0.550 T (highlighted in Figure 3a). Both the CW (red) and CCW (blue) modes start from over-coupling conditions with negative phase gradients. As γ_+ and γ_- increase with B, the CW mode first reaches the critical point at a B value of 0.072 T alongside an undefined phase gradient characteristic, while the CCW mode is still over-coupled. $S_{21}(f_{21}) = -36.9$ dB and $\Delta f = 20$ MHz

Table 1. Comparison between topological and conventional on-chip isolators.

No.	Platform	Mechanism	Wavelength λ	Isolation ratio [dB]	Chip loss [dB]	Cavity size [λ^2]	Active control	Topological protection against sharp bends and fabrication disorders
(1)[2]	Si	MO[a)]	1550 nm	19.5	6 + GCL[c)]	$841\pi + 7482$	N	N
(2)[20]	Si	nonlinearity	1541 nm	20.3	1.1 + GCL	$\approx 19 \times 13$	N	N
(3)[5]	Si_3N_4	MO	1570 nm	28	2.3 + GCL	382.2×63.7	N	N
(4)[12]	Si	AO[b)]	1550/ 780 nm	39.3	10/14	$\approx 451 \times 258$	N	N
(5)[15]	Si_3N_4	AO	1550 nm	10	(0.1 to 1) + GCL	$\approx 2664\pi$	Electric	N
(6)[13]	Si	AO	1524 nm	16	6 + GCL	$\approx 165 \times 1$[d)]	Electric	N
(7)[6]	Si	MO	638 µm	52	21	$\approx 17 \times 9$	Thermal	N
This work	Si	MO	882 µm	64.3	2.6	6.4×2.5	Optical	Y

[a)] MO: Magneto-optical; [b)] AO: Acousto-optical; [c)] GCL: Grating Coupler Loss: >10 dB; and [d)] Single waveguide without cavity.

at $B = 0.218$ T. When B further increases to 0.550 T, the CCW mode reaches its critical point while CW mode gradually transitions into a deep under-coupling regime, with $S_{12}(f_{12}) = -59.4$ dB and $\Delta f = 52$ MHz.

We further conduct experimental sweeps of the InSb position on the silicon chip to showcase the V_{InSb}-dependent non-reciprocity. The experimental setup is shown in Figure 3d where a rectangular InSb sample is mechanically moved in the xy-plane. Its position displacements along the x- and y- directions are indicated by w and m, and O (0, 0) represents the top left corner of the parallelogram topological cavity. $(w, m) = (0, 0)$ corresponds to the overlap between the bottom left corner of the InSb crystal and the point O. Figure 3e,f illustrates the CW isolation ratio and Δf at B = 0.586 T, respectively. The compact scan area is $9.9 \times 0.66\lambda^2$, with w ranging from −4 to 5 mm and m ranging from −0.3 to 0.3 mm. A critical line of maximum isolation ratio is observed in Figure 3e, where the V_{InSb} ensures critical points as $\gamma_i + \gamma_0 + \gamma_{MO+} = \gamma_c$. Δf reaches the maximum when the InSb primarily overlaps with the straight top arm of the cavity, with $q_{\pm}$ being maximally enhanced. These results provide guidance for precise alignment (e.g., using bonding techniques) in fabricating topological isolator devices. In Particular, the overlap between the critical line and the region of maximum Δf indicates an isolator with both a high isolation ratio and an optimized isolation background. This isolation ratio map is also tunable by adjusting B, further enhancing versatile device integrations. Additional V_{InSb}-dependent results when changing the z-directional gaps are presented in Section S4 (Supporting Information). The V_{InSb}-dependent results for topological waveguides are shown in Section S5 (Supporting Information).

2.3. All-Optical Control of Isolation Ratio

The silicon non-reciprocal chip allows for all-optical active control of isolation ratios. Experimentally, a 525 nm laser is focused on the silicon side of the topological isolator chip, as shown in the inset of **Figure** 4a. The laser beam is incident obliquely onto the sample, focusing near the top arm of the topological cavity. The photoexcited carriers and the optothermal effects introduce active losses $\gamma_p(F)$ so that the total intrinsic cavity loss is modified as $\gamma_i + \gamma_{\pm} + \gamma_p(F)$, where F is the optical flux. The non-reciprocal coupling condition is thus actively tunable with a fixed $B = 0.55$ T, as shown by the measurement results of $S_{12} - S_{21}$ versus F at f_{12} (blue) and f_{21} (red). CW mode begins at critical point with an isolation ratio of 48.0 dB while CCW mode starts in under-coupling condition with an isolation ratio of 16.6 dB. The increasing $\gamma_p(F)$ drives the system into a further under-coupled regime exhibiting an attenuated isolation ratio, which is fully quenched at pumping flux above 1.0×10^5 W m^{-2}. In contrast, the isolation is zero in the absence of the InSb wafer (gray).

By tuning the initial states (zero pump) of CW and CCW modes into the over-coupling regime through adjusting V_{InSb}, we actively tune the non-reciprocal isolation ratio from 0 to its maximum and back to 0 through optical pumping. As demonstrated in Figure 4b, the CCW (blue) and CW (red) modes reach their critical points at F values of 1.02×10^5 and 1.11×10^5 W m^{-2}, respectively, and return to zero as F continuously increases, similar to Figure 4a. The reference zero isolation ratio for the cavity without InSb is also presented (gray). The transmittance and phase spectra for this 0-max-0 modulation are detailed in Figure 4c,d, corresponding to F values of 0.54×10^5, 1.02×10^5, 1.11×10^5, and 1.61×10^5 W m^{-2}. Both the CW mode (S_{21} in red) and CCW mode (S_{12} in blue) transition from over-coupling to critical-coupling and under-coupling conditions, as the phase gradients vary from negative to undefined, and to positive. The CW and CCW critical points are highlighted in the mid-two panels ($F = 1.02 \times 10^5$ and 1.11×10^5 W m^{-2}) of Figure 4c,d, respectively. The non-reciprocity is also completely suppressed at high pumping flux (1.61×10^5 W m^{-2}) in the right panel with overlapped S_{21} and S_{12}. This possibly results from the photoexcited carriers in InSb that break the non-reciprocity, as the pumping energy penetrates the VPC slab. Versatile non-reciprocity trends are achievable through precise positioning of the InSb crystal. Additionally, this Si-based non-reciprocal topological chip can be potentially integrated with CMOS-based modulators[40] for high-speed non-reciprocal modulation of signals.

3. Conclusion

We have experimentally demonstrated a compact and low-loss non-reciprocal topological silicon chip. A valley-conserved

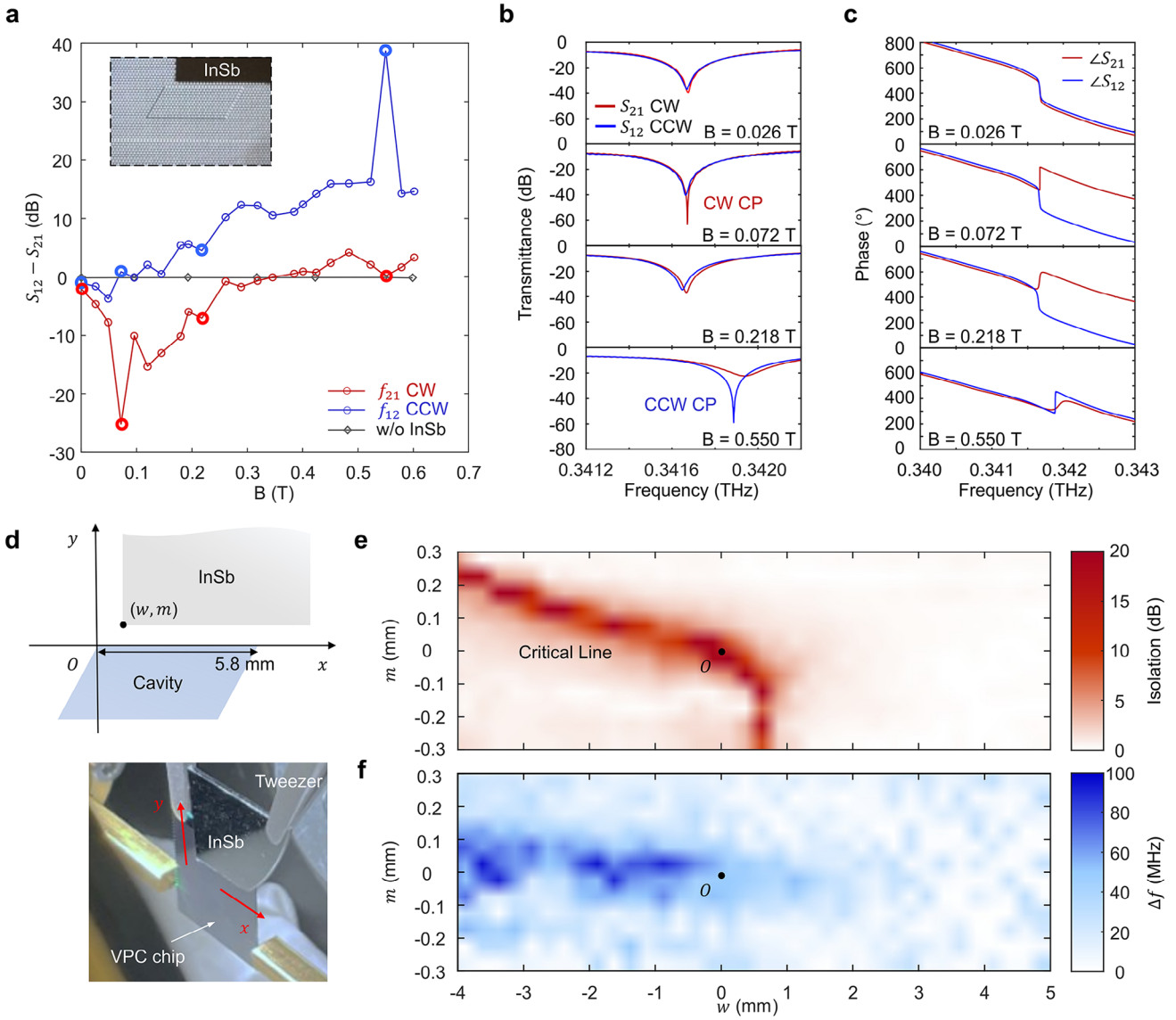

Figure 3. Non-reciprocal critical points and position-dependent isolation ratio. a) Experimental $S_{12} - S_{21}$ versus magnetic field B. Both CW (red) and CCW (blue) critical points are obtained at respective resonant frequencies f_{21} and f_{12}, respectively, with B from 0 to 0.62 T. Zero isolation ratios are observed for cavities without InSb (gray). The sample image is shown in the inset. b,c) Experimental transmittances and phases for B values of 0.026, 0.072, 0.218, and 0.55 T, respectively, with non-reciprocal critical points highlighted. d) Experimental setup to test position-dependent non-reciprocity. InSb wafer is mechanically moved near the upper arm of the topological cavity. x- and y-directional displacements are indicated by w and m, respectively. e, f) Experimental CW isolation ratio (red) and frequency detuning (blue) through shifting the position of the InSb wafer. A critical coupling line is observed in (e).

non-reciprocal mode is realized for the first time by aligning magneto-optical InSb with the valley-Hall topological waveguide and waveguide-cavity, breaking both spatial and temporal reversal symmetries. Our topological non-reciprocal chip achieves a maximum isolation ratio of 64.3 dB based on the tunable non-reciprocal critical coupling condition. It also exhibits an extremely low chip loss of 2.6 dB and a compact cavity footprint at $6.4 \times 2.5\lambda^2$, significantly outperforming conventional isolators. Additionally, we showcase active control of the isolation ratio using an all-optical method, achieving a controllable isolation ratio ranging up to 48 dB. This experimental demonstration provides a route for advancing non-reciprocal topological photonics, with potential applications in terahertz communication technologies, LiDAR chips, quantum computers, and secure communication networks.

4. Experimental Section

Sample Fabrication: The terahertz VPC chips were fabricated on a 6-inch-diameter high-resistivity (≈20 kΩ•cm) silicon wafer with a thickness of 500 µm. A 2-µm-thick silicon dioxide layer was deposited on top of the wafer. The photoresist was spin-coated and patterned using photolithography, followed by reactive ion etching to etch the silicon dioxide layer. Deep reactive ion etching was then performed on the silicon, realizing the

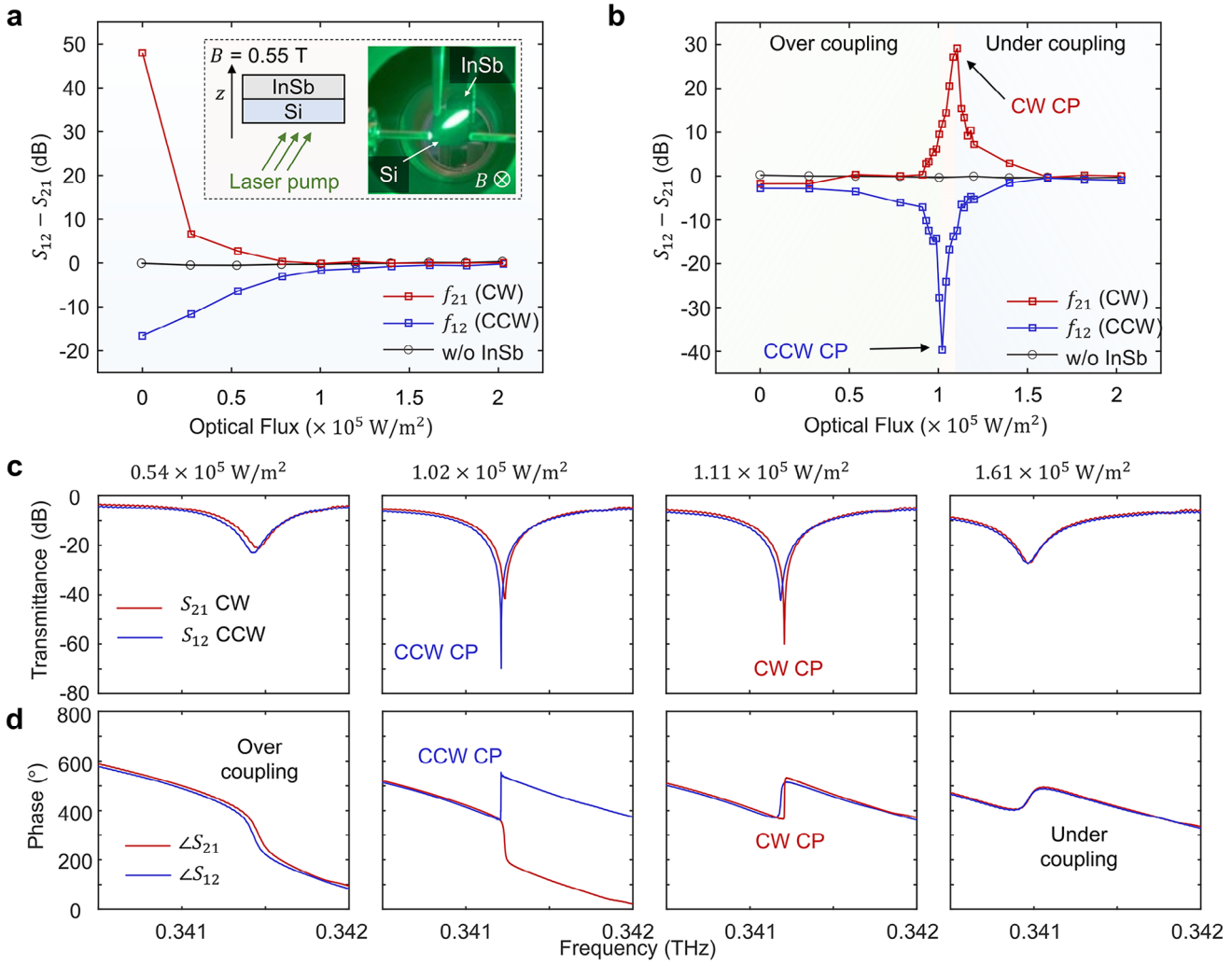

Figure 4. All-optical active on-chip non-reciprocal topological photonic device. a) Experimental active isolation ratio versus optical pumping flux. Red and blue curves indicate $S_{12} - S_{21}$ at CW and CCW resonance frequencies, f_{21} and f_{12}, respectively, in comparison to the zero isolation without InSb (gray). Schematic and image of the experimental setup are shown in the inset, where oblique incident laser pumps silicon under magnetic field $B = 0.55$ T. b) Experimental results of active critical points for CW (red) and CCW (blue) modes. The isolation ratio is actively tuned from 0 to max, and to 0. c,d) Transmittance and phase spectra versus optical flux of 0.54 × 10^5, 1.02 × 10^5, 1.11 × 10^5, and 1.61 × 10^5 W m^{-2}, respectively.

etching depth of over 280 µm. Back-grinding was utilized to reduce the thickness to 190 µm. The InSb was diced from a 2-inch wafer with a thickness of 500 µm and crystal orientation of ⟨100⟩. The carrier concentration is from 3 × 10^{14} to 3 × 10^{15} cm^{-3} at 77 K. The charge carrier mobility is >4 × 10^5 cm^2/(V·s). The polished side was attached to the silicon VPC chip.

Experimental Setup: The terahertz signal was generated and received using a Keysight N5222B Vector Network Analyzer (VNA), equipped with two frequency extension modules (Z-325 and Z-500 type) operating within the 325–500 GHz frequency band. The terahertz wave was coupled into and out of the silicon chips via standard WR 2.2 hollow waveguides, facilitated by the taper couplers affixed to the silicon VPC chips. The VNA was calibrated using the standard SOLT (Short, Open, Load, and Through) waveguide calibration procedure, after which the complex S-parameters were measured. An electromagnet (Phywe, 06480-01) was integrated to achieve magnetic bias and controlled by a direct current power supplier (Kepco Power Supply BOP36-28MG). The maximum applied magnetic field was 0.632 T. A 525 nm fiber-coupled diode laser (STHL-525-6-105) was employed for all-optical control of the isolation ratio, utilizing photon energy (2.4 eV) larger than the silicon bandgap (1.1 eV). The laser beam is obliquely incident onto the silicon side of the topological isolator chips, due to the space constraints between the electromagnets. The Si-VPC and InSb were held by two tweezers when sweeping the V_{InSb}, movable through 3D moving stages. The minimum distance step in Figure 3e,f is 50 µm.

Numerical Analysis: The band diagram of the topological edge state was simulated using the finite-element method (COMSOL Multiphysics), where the material layered on top of the silicon VPC possesses different effective permittivities along ±x-directions. The simulated field profile of the topological cavity was obtained using the time domain solver with finite integration theory (CST Studio Suite). Data processing was performed in MATLAB.

Supporting Information

Supporting Information is available from the Wiley Online Library or from the author.

Acknowledgements

The authors acknowledge the research funding supported by the National Research Foundation Singapore, Grant No.: NRF-CRP23-2019-0005, and by National Research Foundation Singapore, Grant No.: NRF-MSG-2023-0002. The authors also acknowledge the advanced sample fabrication performed by the Nanyang NanoFabrication Centre at Nanyang Technological University in Singapore. The authors also acknowledge Disco Hi-Tec Pte Ltd in Singapore for the grinding services provided.

Conflict of Interest

The authors declare no conflict of interest.

Author Contributions

R.J. and R.S. conceived the idea and planned the experiments. R.J. performed the numerical analysis with the help of W.W. and Y.J.T. R.J. performed the measurement with the help of T.C.T and S.S.M. R.J. and R.S. wrote the paper with inputs from all the authors. R.S. led the overall project.

Data Availability Statement

The data that support the findings of this study are available from the corresponding author upon reasonable request.

Keywords

active non-reciprocity, non-reciprocal critical coupling state, on-chip integrated isolator, silicon photonics, terahertz topological isolator, terahertz topological photonic integrated circuits, topological non-reciprocity, topological waveguide, topological cavity

Received: January 24, 2025
Revised: March 19, 2025
Published online: April 10, 2025

[1] Z. Wang, Y. Chong, J. D. Joannopoulos, M. Soljačić, *Nature* **2009**, *461*, 772.
[2] L. Bi, J. Hu, P. Jiang, D. H. Kim, G. F. Dionne, L. C. Kimerling, C. A. Ross, *Nat. Photonics* **2011**, *5*, 758.
[3] K. Fang, Z. Yu, S. Fan, *Nat. Photonics* **2012**, *6*, 782.
[4] B. Bahari, A. Ndao, F. Vallini, A. El Amili, Y. Fainman, B. Kanté, *Science* **2017**, *358*, 636.
[5] W. Yan, Y. Yang, S. Liu, Y. Zhang, S. Xia, T. Kang, W. Yang, J. Qin, L. Deng, L. Bi, *Optica* **2020**, *7*, 1555.
[6] S. Yuan, L. Chen, Z. Wang, W. Deng, Z. Hou, C. Zhang, Y. Yu, X. Wu, X. Zhang, *Nat. Commun.* **2021**, *12*, 5570.
[7] Z. Tan, F. Fan, D. Zhao, H. Wang, S. Li, S. Guan, J.-R. Cheng, Y. Ji, S. Chang, *Laser Photonics Rev.* **2024**, *18*, 2301008.
[8] S. Yang, M. Liu, C. Zhao, S. Fan, C.-W. Qiu, *Nat. Photonics* **2024**, *18*, 412.
[9] M. S. Kang, A. Butsch, P. S. J. Russell, *Nat. Photonics* **2011**, *5*, 549.
[10] J. Kim, S. Kim, G. Bahl, *Sci. Rep.* **2017**, *7*, 1647.
[11] D. B. Sohn, S. Kim, G. Bahl, *Nat. Photonics* **2018**, *12*, 91.
[12] D. B. Sohn, O. E. Örsel, G. Bahl, *Nat. Photonics* **2021**, *15*, 822.
[13] E. A. Kittlaus, W. M. Jones, P. T. Rakich, N. T. Otterstrom, R. E. Muller, M. Rais-Zadeh, *Nat. Photonics* **2021**, *15*, 43.
[14] F. Ruesink, M.-A. Miri, A. Alù, E. Verhagen, *Nat. Commun.* **2016**, *7*, 13662.
[15] H. Tian, J. Liu, A. Siddharth, R. N. Wang, T. Blésin, J. He, T. J. Kippenberg, S. A. Bhave, *Nat. Photonics* **2021**, *15*, 828.
[16] J. A. Kong, *Proc. IEEE* **1972**, *60*, 1036.
[17] D. L. Sounas, A. Alù, *Nat. Photonics* **2017**, *11*, 774.
[18] L. Chang, X. Jiang, S. Hua, C. Yang, J. Wen, L. Jiang, G. Li, G. Wang, M. Xiao, *Nat. Photonics* **2014**, *8*, 524.
[19] Y. Shi, Z. Yu, S. Fan, *Nat. Photonics* **2015**, *9*, 388.
[20] K. Y. Yang, J. Skarda, M. Cotrufo, A. Dutt, G. H. Ahn, M. Sawaby, D. Vercruysse, A. Arbabian, S. Fan, A. Alù, J. Vučković, *Nat. Photonics* **2020**, *14*, 369.
[21] P. Dong, Y.-K. Chen, G.-H. Duan, D. T. Neilson, *Nanophotonics* **2014**, *3*, 215.
[22] J. Ma, X. Xi, X. Sun, *Laser Photonics Rev.* **2019**, *13*, 1900087.
[23] A. Kumar, M. Gupta, P. Pitchappa, N. Wang, M. Fujita, R. Singh, *J. Appl. Phys.* **2022**, *132*, 140901.
[24] A. W. Elshaari, W. Pernice, K. Srinivasan, O. Benson, V. Zwiller, *Nat. Photonics* **2020**, *14*, 285.
[25] M. Wang, R.-Y. Zhang, L. Zhang, D. Wang, Q. Guo, Z.-Q. Zhang, C. T. Chan, *Phys. Rev. Lett.* **2021**, *126*, 067401.
[26] G.-J. Tang, X.-T. He, F.-L. Shi, J.-W. Liu, X.-D. Chen, J.-W. Dong, *Laser Photonics Rev.* **2022**, *16*, 2100300.
[27] X.-T. He, E.-T. Liang, J.-J. Yuan, H.-Y. Qiu, X.-D. Chen, F.-L. Zhao, J.-W. Dong, *Nat. Commun.* **2019**, *10*, 872.
[28] Y. Yang, Y. Yamagami, X. Yu, P. Pitchappa, J. Webber, B. Zhang, M. Fujita, T. Nagatsuma, R. Singh, *Nat. Photonics* **2020**, *14*, 446.
[29] H. Xue, Y. Yang, B. Zhang, *Adv. Photonics Res.* **2021**, *2*, 2100013.
[30] Y. Chen, X.-T. He, Y.-J. Cheng, H.-Y. Qiu, L.-T. Feng, M. Zhang, D.-X. Dai, G.-C. Guo, J.-W. Dong, X.-F. Ren, *Phys. Rev. Lett.* **2021**, *126*, 230503.
[31] A. Kumar, M. Gupta, P. Pitchappa, N. Wang, P. Szriftgiser, G. Ducournau, R. Singh, *Nat. Commun.* **2022**, *13*, 5404.
[32] R. Jia, S. Kumar, T. C. Tan, A. Kumar, Y. J. Tan, M. Gupta, P. Szriftgiser, A. Alphones, G. Ducournau, R. Singh, *Sci. Adv.* **2023**, *9*, adi8500.
[33] M. Gupta, A. Kumar, P. Pitchappa, Y. J. Tan, P. Szriftgiser, G. Ducournau, R. Singh, *Adv. Mater.* **2024**, *36*, 2309497.
[34] L. He, D. Liu, H. Zhang, F. Zhang, W. Zhang, X. Feng, Y. Huang, K. Cui, F. Liu, W. Zhang, X. Zhang, *Adv. Mater.* **2024**, *36*,2311611.
[35] W. Wang, Y. J. Tan, T. C. Tan, A. Kumar, P. Pitchappa, P. Szriftgiser, G. Ducournau, R. Singh, *Nature* **2024**, *632*, 522.
[36] T. Ma, G. Shvets, *New J. Phys.* **2016**, *18*, 025012.
[37] R. Jia, Y. J. Tan, N. Navaratna, A. Kumar, R. Singh, *Adv. Mater.* **2025**, *37*, 2415083.
[38] J. R. Schaibley, H. Yu, G. Clark, P. Rivera, J. S. Ross, K. L. Seyler, W. Yao, X. Xu, *Nat. Rev. Mater.* **2016**, *1*, 16055.
[39] A. Kumar, M. Gupta, P. Pitchappa, T. C. Tan, U. Chattopadhyay, G. Ducournau, N. Wang, Y. Chong, R. Singh, *Adv. Mater.* **2022**, *34*, 2202370.
[40] G. T. Reed, G. Mashanovich, F. Y. Gardes, D. J. Thomson, *Nat. Photonics* **2010**, *4*, 518.